Sound Speed Estimation for Distributed Aberration Correction in Laterally Varying Media

Rehman Ali, Trevor M. Mitcham, Melanie Singh, Marvin M. Doyley, *Senior Member, IEEE*, Richard R. Bouchard, Jeremy J. Dahl, *Senior Member, IEEE*, and Nebojsa Duric

***Abstract*—Spatial variation in sound speed causes aberration in medical ultrasound imaging. Although our previous work has examined aberration correction in the presence of a spatially varying sound speed, practical implementations were limited to layered media due to the sound speed estimation process involved. Unfortunately, most models of layered media do not capture the lateral variations in sound speed that have the greatest aberrative effect on the image. Building upon a Fourier split-step migration technique from geophysics, this work introduces an iterative sound speed estimation and distributed aberration correction technique that can model and correct for aberrations resulting from laterally varying media. We first characterize our approach in simulations where the scattering in the media is known a-priori. Phantom and in-vivo experiments further demonstrate the capabilities of the iterative correction technique. As a result of the iterative correction scheme, point target resolution improves by up to a factor of 4 and lesion contrast improves by up to 10.0 dB in the phantom experiments presented.**

***Index Terms*—Aberration correction, Fourier split-step, medical ultrasound, migration velocity analysis, Ray tomography.**

Manuscript received 11 October 2022; revised 8 January 2023 and 10 March 2023; accepted 20 March 2023. Date of publication 28 March 2023; date of current version 13 April 2023. This work was supported by the Stanford-Philips Research Collaboration, the University of Rochester Medical Center, and the National Institute of Biomedical Imaging and Bioengineering (NIBIB) under Grants R01-EB027100 and R01-EB028652. The associate editor coordinating the review of this manuscript and approving it for publication was Dr. Gregery T. Buzzard. *(Corresponding author: Rehman Ali.)*

This work involved animals in its research. Approval of all ethical and experimental procedures and protocols was granted by Stanford University's Institutional Administrative Panel on Laboratory Animal Care.

Rehman Ali and Trevor M. Mitcham are with the Department of Imaging Sciences, University of Rochester Medical Center, Rochester, NY 14642 USA (e-mail: rehman_ali@urmc.rochester.edu; Trevor_Mitcham@URMC.Rochester.edu).

Melanie Singh is with the Department of Biomedical Engineering, University of Rochester, Rochester, NY 14627 USA (e-mail: melaniesingh@rochester.edu).

Marvin M. Doyley is with the Department of Electrical Engineering, University of Rochester, Rochester, NY 14627 USA (e-mail: m.doyley@rochester.edu).

Nebojsa Duric is with the Department of Imaging Sciences, University of Rochester Medical Center, Rochester, NY 14642 USA, and also with the Department of Electrical Engineering, University of Rochester, Rochester, NY 14627 USA (e-mail: nebojsa_duric@urmc.rochester.edu).

Richard R. Bouchard is with the Department of Imaging Physics, University of Texas MD Anderson Cancer Center, Houston, TX 77030 USA (e-mail: rrbouchard@mdanderson.org).

Jeremy J. Dahl is with the Department of Radiology, Stanford University School of Medicine, Stanford, CA 94305 USA (e-mail: jeremy.dahl@stanford.edu).

Digital Object Identifier 10.1109/TCI.2023.3261507

I. Introduction

PHASE aberration is one of the main sources of image degradation in medical pulse-echo ultrasound and is ultimately caused by spatial variations in the sound speed of tissue. Although the acoustic sound speed can vary by up to 10% in soft tissues [1] there is a lack of robust techniques that can effectively estimate the sound speed to then correct for aberrations in the ultrasound image. Instead, most phase aberration correction techniques used in pulse-echo ultrasound rely on phase screen models which assume that all aberrations can be captured by a single thin-film at the transducer surface [2], [3], [4]. However, spatial variations in the speed of sound cause a spatially varying set of delays and diffractive effects that a thin-film phase screen at the transducer does not adequately model.

Recent work [5], [6], [7], [8] in medical ultrasound imaging has adapted the Fourier split-step migration technique from geophysics to aberration correction based on the sound speed profile in tissue. However, the practical application of this technique is hindered by the lack of prior knowledge of the sound speed profile in tissue. Several sound speed estimators have been proposed for medical pulse-echo ultrasound [9], [10], [11], [12] with the significant majority of estimators focused on estimating a single global average sound speed value applicable to the entire image [13], [14], [15], [16]. Instead of directly attempting a distributed estimation, some works extend the global average sound speed estimators to reconstruct the axial profile of sound speed in layered media by relating depth-wise measurements of the average sound speed to the local sound speed [17], [18], [19], [20]. These later works are similar to Dix inversion from seismic imaging where the interval velocity is deduced from the optimal stacking velocity at different imaging depths [21].

Recent sound speed estimators have explored using ray tomography to reconstruct sound speed based on time-of-flight differences observed from shifts in the ultrasound image [10], [12]. Unlike the previous sound speed estimators which were limited to applications with a depth-varying sound speed, these tomographic estimators reconstruct lateral variations in sound speed; however, the major challenge of this approach is its ill-posed nature [22], [23], [24], which arises from ambiguities in the depth placement of the imaging target [25], [26], [27], [28]. As a result, tomographic estimators struggle to accurately estimate the depth-varying component or the global average sound speed without first applying some kind of calibration in combination with regularization to penalize the lateral gradient of the sound speed reconstruction [29].

But this is no problem because mainly the lateral variations are important for aberration correction, not the axial ones [9], [30], [31], [32]. For this reason, we investigate a tomographic sound speed estimator in conjunction with Fourier split-step migration to correct for aberrations in the ultrasound image. By using the Fourier split-step method to correct for aberration, this work presents a transition towards the application of waveform tomography in handheld pulse-echo ultrasound [33]. While most of the prior literature uses a single set of observed aberration delays or phase shifts to reconstruct sound speed, we use an iterative procedure in which aberrations in the image are used to reconstruct the sound speed profile, which is in turn used to re-image the medium, estimate a new set of aberration delays, and update the sound speed profile in the medium.

In this paper, our goals are three-fold: a) introduce a new iterative model-based tomographic sound speed estimator sufficient for aberration correction in the ultrasound image; b) demonstrate how the depth ambiguity of the reflector impacts the sound speed estimate; and c) provide open-source code and data that will allow the broader research community to expand and improve upon these ideas. This work will ultimately show that: 1) a nonlinear wavefield solver based on the Fourier-split-step method can be used to estimate time delays between different transmit events; 2) the resulting time delay estimates can be combined with a linear solver that uses ray tracing to reconstruct sound speed; 3) an iterative approach where previous iterations inform subsequent iterations can lead to slow but significant improvements in image quality; and 4) aberration correction does not necessarily require perfect sound speed estimation to be effective.

II. Theory

A. Fourier Split-Step Angular Spectrum Method

Ultrasonic wave-fields $p(x, z, f)$ as a function of two-dimensional location (x, z) and frequency f can be propagated from a depth of z to $z + \Delta z$ using the Fourier split-step method [5], [6], [7], [8], [34]:

$$p(x, z + \Delta z, f) = W(x) S_{\pm}(x, z, f) \mathcal{F}^{-1}_{k_x \mapsto x} H_{\pm}(k_x, z, f) \mathcal{F}_{x \mapsto k_x} p(x, z, f), \tag{1}$$

$$H_{\pm}(k_x, z, f) = \exp\left(\pm j 2\pi \left(\frac{f^2}{\bar{c}^2(z)} - k_x^2 \right)^{1/2} \Delta z \right), \tag{2}$$

$$S_{\pm}(x, z, f) = \exp\left(\pm \frac{j 2\pi f \Delta z}{c_{res}(x, z)} \right), \tag{3}$$

$$\frac{1}{\bar{c}(z)} = \frac{1}{L} \int_{-L/2}^{L/2} \frac{dx}{c(x, z)}, \tag{4}$$

$$\frac{1}{c_{res}(x, z)} = \frac{1}{c(x, z)} - \frac{1}{\bar{c}(z)}, \tag{5}$$

where $\mathcal{F}_{x \mapsto k_x}$ and $\mathcal{F}^{-1}_{k_x \mapsto x}$ are the forward and inverse Fourier transforms in the lateral dimension (x), $W(x)$ is an anti-aliasing window used to suppress wrap-around in the lateral dimension, $c(x, z)$ is the sound speed in the medium, and L is the lateral length of the computational domain over which the angular spectrum method is applied. Because this is a Fourier split-step scheme, we decompose $c(x, z)$ into an axially varying component $\bar{c}(z)$ and a laterally varying component $c_{res}(x, z)$: $H_{\pm}$ is bulk propagation via the angular spectrum method at a sound speed $\bar{c}(z)$, and $S_{\pm}$ is a phase screen correction involving the laterally varying part $c_{res}(x, z)$.

B. Imaging by Correlation of Transmit and Receive Wavefields

Pulse-echo ultrasound images can be created by propagating transmit and receive wavefields $p_{tx(i)}(x, z, f)$ and $p_{rx(i)}(x, z, f)$ based on the receive channel data collected from pulses emitted by each transmit element $i = 1, \ldots, N$. Partial images $I_i(x, z)$ can be formed prior to amplitude detection based on the following equations:

$$I_i(x, z) = \int_0^{\infty} p^*_{tx(i)}(x, z, f) p_{rx(i)}(x, z, f) df, \tag{6}$$

$$p_{tx(i)}(x, z + \Delta z, f) = W(x) S_{-}(x, z, f) \mathcal{F}^{-1}_{k_x \mapsto x} H_{-}(k_x, z, f) \mathcal{F}_{x \mapsto k_x} p_{tx(i)}(x, z, f), \tag{7}$$

$$p_{rx(i)}(x, z + \Delta z, f) = W(x) S_{+}(x, z, f) \mathcal{F}^{-1}_{k_x \mapsto x} H_{+}(k_x, z, f) \mathcal{F}_{x \mapsto k_x} p_{rx(i)}(x, z, f), \tag{8}$$

Propagation via the Fourier split-step angular spectrum method should correct for aberration by accounting for the true sound speed in the medium. The B-mode image $I_{BMode}(x, z)$ is obtained by coherently compounding images $I_i(x, z)$, applying amplitude detection to the result of coherent compounding, and decibel-scaling the amplitude-detected result:

$$I_{BMode}(x, z) = 20 \log_{10} \left| \sum_{i=1}^{N} I_i(x, z) \right|. \tag{9}$$

C. Aberration Delay Estimation

Equation (6) is augmented to include a time axis t:

$$I_i(x, z; t) = \int_0^{\infty} p^*_{tx(i)}(x, z, f) p_{rx(i)}(x, z, f) e^{j 2\pi f t} df, \tag{10}$$

such that the aberration delay t_d between I_i and I_{i+1} at each point (x, z) is found by maximizing the time-domain correlation between $I_i(x, z; t)$ and $I_{i+1}(x, z; t - t_d)$ using a phase shift method [35]. The creation of a time axis distinct from the spatial coordinates of the image avoids the cosine dependence shown in [11], [22] for the conversion of spatial shifts in the image to errors in the time-of-flight. This approach has also been used in seismic imaging to directly measure the time shift between imaged reflections and is known as the “time-shift imaging condition” [36].

D. Reconstruction of Sound Speed From Estimated Delays

The reconstruction of sound speed $c(x,z)$ from estimated delays is a ray tomography problem that uses line integrals over the slowness profile to reconstruct the slowness (i.e., the reciprocal of sound speed):

$$\vec{t}_d = \boldsymbol{D}\boldsymbol{A}\Delta\vec{s}, \tag{11}$$

where $\Delta\vec{s}$ is a vectorization of $\frac{1}{c(x,z)} - \frac{1}{c_{prior}(x,z)}$ ($c_{prior}(x,z)$ is the previous estimate of sound speed, so $\Delta\vec{s}$ is an update to $1/c_{prior}$), $\boldsymbol{A}$ is a matrix that encodes line integrals between every transmit element and imaging point, $\boldsymbol{D}$ is a matrix that calculates the differences between the times-of-flight from neighboring transmit elements, and $\vec{t}_d$ is a vector of delay estimates observed between pairs of images I_i and I_{i+1} corresponding to each transmit element. Unlike our prior work involving coherence-based sound speed estimates [9], the ray tomography used in this work relies on differences ($\boldsymbol{D}$) between the times-of-flight to an imaging point rather than the absolute time-of-flight. The following least-squares problem is used to reconstruct the update $\Delta\vec{s}$ to the slowness image:

$$\min_{\vec{s}} \left\{ \frac{1}{2}(\vec{t}_d - \boldsymbol{D}\boldsymbol{A}\Delta\vec{s})^T \boldsymbol{R}^{-1}(\vec{t}_d - \boldsymbol{D}\boldsymbol{A}\Delta\vec{s}) + \frac{1}{2}\Delta\vec{s}^T \boldsymbol{Q}^{-1}\Delta\vec{s} \right\}, \tag{12}$$

where the residual $\vec{t}_d - \boldsymbol{D}\boldsymbol{A}\Delta\vec{s}$ is modeled as a normal random variable with mean $\vec{0}$ and covariance $\boldsymbol{R}$ (a diagonal matrix whose entries are proportional to the mean path length [9]), and the slowness update image $\Delta\vec{s}$ is modeled as a normal random variable with mean $\vec{0}$ and covariance $\boldsymbol{Q}$. The covariance $\boldsymbol{Q}$ is modeled as a weighted sum of covariance matrices encoding different priors on the slowness image,

$$\boldsymbol{Q} = \gamma \boldsymbol{Q_{blur}} + (1-\gamma)\boldsymbol{Q_{layer}} \tag{13}$$

where $\boldsymbol{Q_{blur}}$ is implemented as a convolution with a Gaussian blurring kernel to enforce smoothness, $\boldsymbol{Q_{layer}}$ is implemented as spatial averaging over the lateral dimension to enforce a layered structure in the reconstructed slowness, and $\gamma \in [0,1]$ is the weight given to $\boldsymbol{Q_{blur}}$ relative to $\boldsymbol{Q_{layer}}$ in the overall covariance $\boldsymbol{Q}$. The closed-form solution to the least-squares reconstruction problem (12) is

$$\Delta\vec{s} = \boldsymbol{Q}\boldsymbol{A}^T\boldsymbol{D}^T(\boldsymbol{D}\boldsymbol{A}\boldsymbol{Q}\boldsymbol{A}^T\boldsymbol{D}^T + \boldsymbol{R})^{-1}(\vec{t}_d - \boldsymbol{D}\boldsymbol{A}\Delta\vec{s}), \tag{14}$$

which can be broken into two parts

$$(\boldsymbol{D}\boldsymbol{A}\boldsymbol{Q}\boldsymbol{A}^T\boldsymbol{D}^T + \boldsymbol{R})\xi = \vec{t}_d - \boldsymbol{D}\boldsymbol{A}\Delta\vec{s}, \tag{15}$$

$$\Delta\vec{s} = \boldsymbol{Q}\boldsymbol{A}^T\boldsymbol{D}^T\xi. \tag{16}$$

where ξ is an intermediate term determined by solving (15) using the conjugate gradient method. The resulting ξ is then used in (16) to obtain the slowness update.

E. Iterative Tomography and Image Correction Framework

Ultimately, we employ an iterative scheme to estimate the speed of sound and correct for phase aberrations in the ultrasound image. Equations (6)–(10) are first used to reconstruct images (initially assuming a spatially constant sound speed) to compute aberration delays. Then, (15) and (16) are used to update the speed of sound. This updated sound speed profile is used to recreate the ultrasound image and compute a new set of aberration delays, which is in turn used to compute the next update to the speed of sound. Unlike prior work involving the reconstruction of sound speed from a single set of measured aberration delays [10], [11], [12], this work involves the re-estimation of aberration delays after each new sound speed estimate. This iterative framework for sound speed reconstruction and image correction will be referred to as Iterative Model-based Phase Aberration Correction and Tomography (IMPACT) for the remainder of this work.

III. Methods

A. K-Wave Simulations in Heterogeneous Media

Multistatic synthetic aperture channel data was simulated in k-Wave [38] for diffuse scattering in several heterogeneous sound speed media to evaluate the performance of IMPACT. Six abdominal models [37] (see example in Fig. 1) and 12 additional media with randomized Gaussian aberrators (full width at half maximum of 3.6 mm in both axial and lateral dimension) from 2 to 17 mm depth (see ground truth sound speed maps in Fig. 2) were used to evaluate IMPACT in the presence of several different aberrating sound speed profiles. The mean sound speed inside the aberrators is 1540 m/s, while the sound speed above and below the aberrator is 1560 m/s (similar to the sound speed in the skin and liver). Smooth distributions in the speed of sound were used in each of these phantoms to best control the scattering in the medium and preserve the shape of the imaging target. Sharp transitions in sound speed would create new reflections that would change the shape and appearance of the imaging target.

A 5×5 grid perimeter of point targets (spaced 4.5 mm axially and 3.75 mm laterally) surrounding a 3×3 grid of -6 dB hypoechoic lesions (spaced 4.5 mm axially and laterally) were used in the simulations to quantify the resolution and contrast before and after distributed aberration correction (see Fig. 2 as an example). The Hilbert transform was applied to the multistatic dataset to obtain an analytic representation of the channel signals. All k-Wave simulations used a linear array with 128 elements and 0.2 mm pitch (no kerf), a transmit pulse with 8 MHz center frequency and 70% fractional bandwidth, a 128.33 MHz sampling frequency, and a 0.04 mm grid spacing. The linear array is centered laterally at x = 0 and placed at an axial depth of z = 0 on the imaging grid (see Fig. 1).

B. Experimental Data Acquisition

Hadamard encoded transmit sequences [39] were used to acquire multistatic synthetic aperture datasets both *in vitro* and *in vivo* on the Verasonics Vantage 256 scanner (Verasonics Inc., Kirkland, WA, USA) using the L12-5 50 mm (256 elements; 0.2 mm pitch; 6 MHz center frequency) and L12-3v (192 elements; 0.2 mm pitch; 7.8 MHz center frequency) probes. Phantom experiments were performed in tissue-mimicking gelatin phantoms with the L12-5 50 mm probe, while *in-vivo* datasets

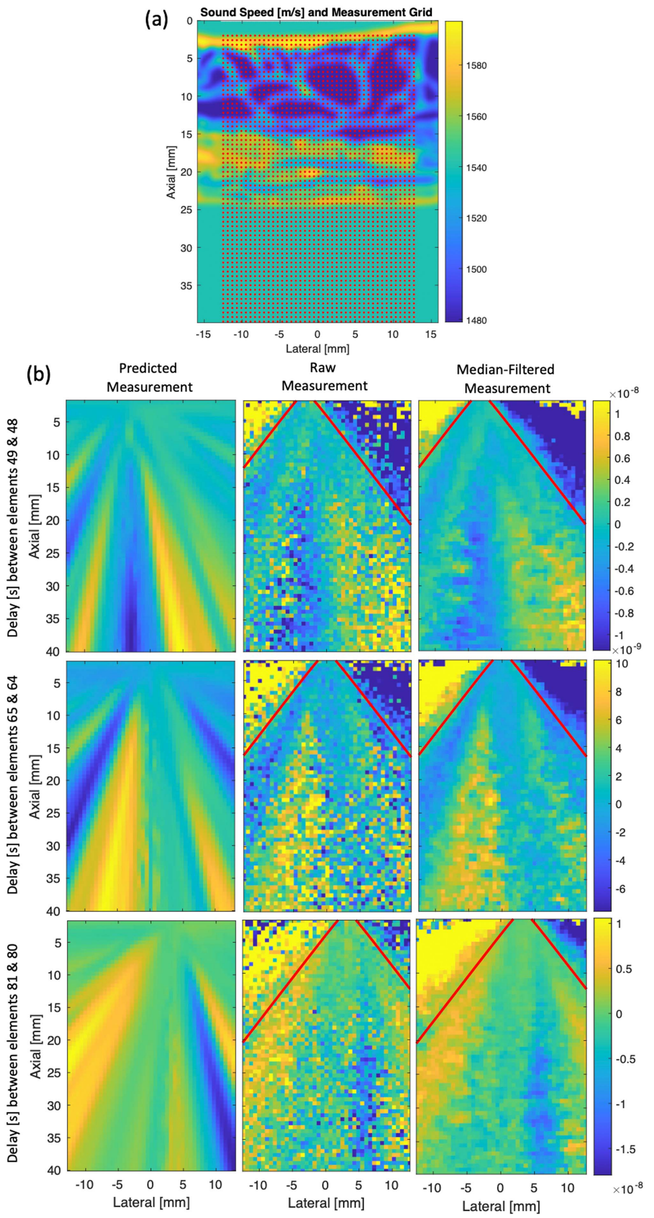

Fig. 1. Median Filtering of Aberration Delays and F-Number Limits. (a) Sound speed map [37] corresponding to the k-Wave simulation used in this demonstration. The red dots indicate the locations where the aberration delay measurements were sampled. (b) Images that show how the median filter was applied to the measured aberration delays and how the f-number limit ($f/1.3$) is used to exclude measurements outside of the region bounded by the red lines. The first column shows the aberration delays predicted by (11) for each element pair (48 & 49, 64 & 65, and 80 & 81). The second column shows the raw measurement of aberration delays, and the third column show the aberration delay measurement after median filtering.

were acquired from the abdomen of obese Zucker rats [40] with the L12-3v probe.

C. Phantom Fabrication

The tissue-mimicking phantom material used in this work was fabricated by cross-linking a mixture of 8% gelatin (Sigma Aldrich, St. Louis, MO, USA), 2.5% silica (US Silica, Katy, TX, USA), 89.4% degassed and deionized water, and 0.1% glutaraldehyde (Sigma Aldrich) [41] in a 4-inch acrylic cube. Either two or three rows of wire targets which consisted of 36-GA (127-μm diameter) copper wire (McMaster-Carr, Elmhurst, IL) were included as imaging targets within all phantoms. Additionally, hypo-echoic lesions consisting of 8% gelatin, 0.5% silica, 91.4% deionized water, and 0.1% glutaraldehyde (i.e., lower silica content compared to the phantom background) were included at the distal boundary of some phantoms to provide diversity in imaging targets. In order to create sound speed variation in the near field, gelatin inclusions with an increased sound speed were also cast above the imaging targets by using a mixture of 8% gelatin, 2.5% silica, 69.4% deionized water, 20% isopropanol, and 0.1% glutaraldehyde [42]. Finally, *ex vivo* porcine abdominal tissue was used to mimic heterogeneous tissue aberrators.

D. Sound Speed Estimation and Phase Aberration Correction

For all simulated datasets, a total of five iterations of IMPACT were used to reconstruct sound speed and correct for aberrations in the image. The impact of the layered medium prior was measured by using γ values of 1.0, 0.5, and 0.25 in (13). Additionally, the initial sound speed model was varied to understand its impact on the sound speed estimate and the robustness of the aberration correction technique. The initial sound speeds used in IMPACT were 1500, 1540, and 1580 m/s. Lastly, for all experimental data acquisitions, a total of ten iterations of IMPACT were used with a $\gamma = 1.0$ (i.e., no layered medium prior) and an initial homogeneous sound speed model of 1540 m/s. The Gaussian blurring kernel used for $\boldsymbol{Q_{blur}}$ had a full-width at half-maximum (FWHM) of 3.0 mm in both in the x- and z-directions.

E. Preprocessing Filters for Aberration Delays Measurements

To implement IMPACT, a median filter is applied to the aberration delay measurement in order to reduce the effect of measurement noise on the tomographic reconstruction process. The filter calculates the median of the aberration delay measurment over a roughly 4.5 $\lambda \times 4.5\ \lambda$ window, where λ is the wavelength at the initial sound speed used at the first iteration of IMPACT. Only aberration delays that fall within an f-number limit of 1.0 (or 1.3 in the k-Wave simulations) are used in $\vec{t}_d$ for the sound speed reconstruction problem. Furthermore, to limit the impact of reverberation clutter on the aberration delay measurement in physical experiments, we implement a direction-of-arrival filter [43] to suppress the presence of extraneous wavefronts. To maximize the correlation between I_i and I_{i+1}, an apodization that maximizes the lag-one coherence (LOC) [44] is applied across the receive aperture prior to Fourier split-step migration. Unlike the common midangle approach [11], the major advantage of this approach is that it does not require the reorganization of received echoes in terms of midangle and angular offset to increase signal correlations. The common midangle approach introduces a dependence on the receive aperture which requires a two-way (transmit-and-receive) modeling of delays. A single consistent receive apodization is used to reduce the problem to a simple one-way (transmit-only) modeling of delays as in [12].

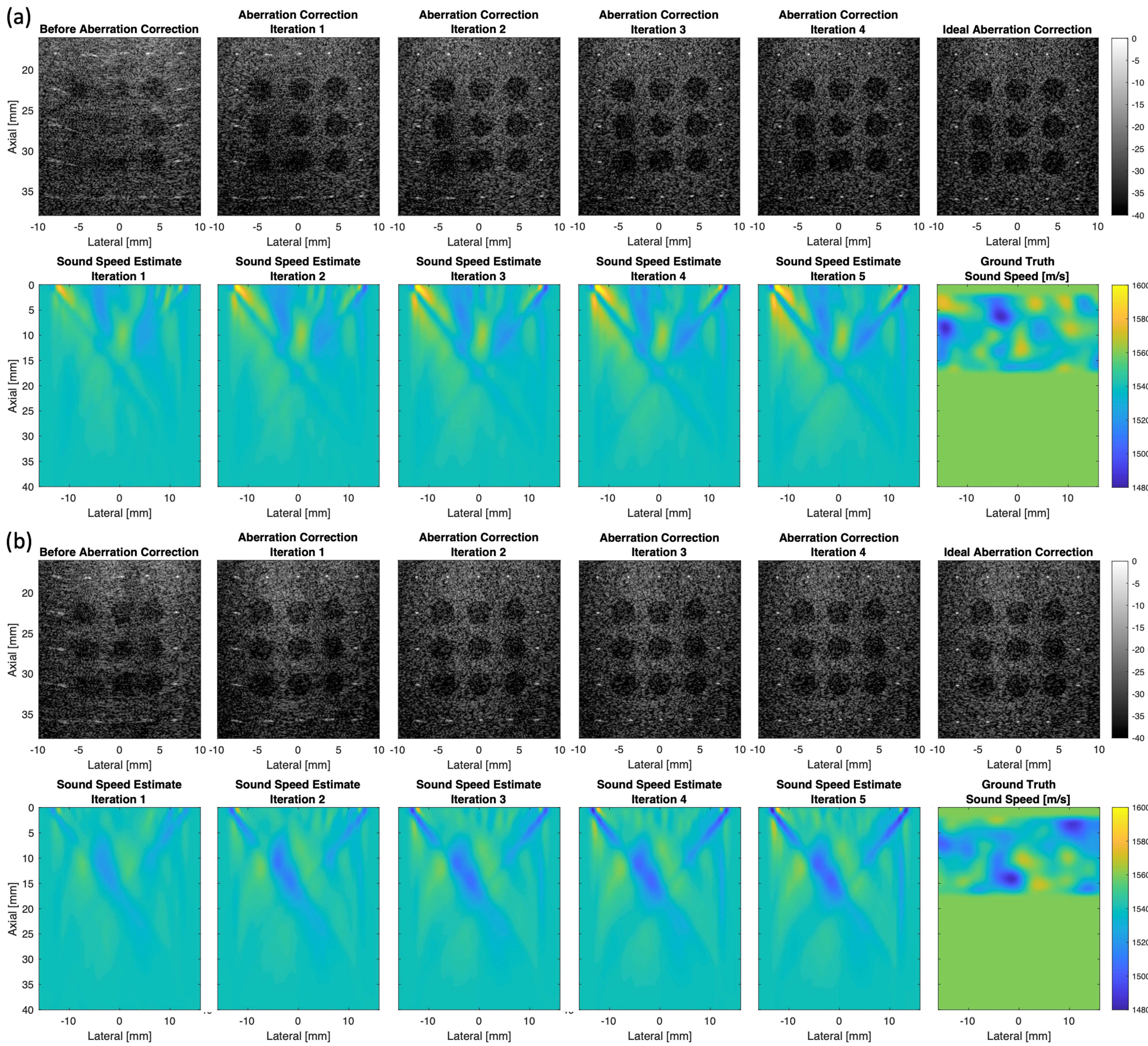

Fig. 2. Demonstration of IMPACT at Each Iteration. The reconstructed ultrasound image and sound speed estimate is shown at each iteration of IMPACT in the absense of a layered medium prior ($\gamma = 1.0$) using two different Gaussian aberrators (a) and (b) simulated in k-Wave. In each case the aberration correction using the sound speed estimate approaches the ideal aberration correction achieved using the ground truth sound speed profile. Mean and standard deviation values for point target resolution and contrast are presented in Table I for $\gamma = 1.0,\ 0.5,\ 0.25$.

F. Metrics and Evaluation

To quantify image quality, we measure the contrast of each hypoechoic lesion relative to its background, and the imaging resolution in terms of the -6 or -20 dB lateral beamwidth of each point target. In terms of the mean (μ) and variance (σ^2) of image values in the target (T) and background (B) regions of interest (ROIs), contrast is defined as

$$\text{Contrast} = 20 \log_{10} \left(\frac{\mu_T}{\mu_B} \right), \qquad (17)$$

The background ROI is always chosen to have the same size and imaging depth as the target ROI.

IV. Results

A. Optimization of Aberration Delay Measurements

Using data from a k-Wave simulation of an abdominal sound speed model [37], Fig. 1 shows the median filtering process used to remove outliers in the measurement process and the f-number limit shown as bounding red lines. The aberration delay maps in Fig. 1(b) show predicted, measured, and median-filtered time delays over the points in the red dots shown in Fig. 1(a) between elements 48 & 49, 64 & 65, and 80 & 81. After the median filtering process shown, only the aberration delay measurements that fall within the f-number limit (between red lines shown) are used during tomography.

TABLE I
RESOLUTION, CONTRAST, AND SOUND SPEED ERROR VS IMPACT ITERATION ACROSS 12 GAUSSIAN RANDOM ABERRATORS

γ	Metrics	Iteration 1	Iteration 2	Iteration 3	Iteration 4	Iteration 5	Ideal
1.0	-6 dB width [mm] at 18 mm depth	1.01±0.91	0.39±0.51	0.27±0.32	0.21±0.05	0.22±0.05	0.20±0.03
	-6 dB width [mm] at 36 mm depth	2.28±1.31	1.06±0.88	0.55±0.37	0.47±0.28	0.47±0.37	0.29±0.02
	Contrast [dB]	3.34±1.26	5.09±0.95	5.50±0.75	5.65±0.69	5.64±0.61	5.73±0.43
0.5	-6 dB width [mm] at 18 mm depth	1.01±0.91	0.39±0.58	0.26±0.27	0.24±0.24	0.21±0.03	0.20±0.03
	-6 dB width [mm] at 36 mm depth	2.28±1.31	0.93±0.82	0.50±0.33	0.46±0.42	0.34±0.15	0.29±0.02
	Contrast [dB]	3.34±1.26	5.34±0.78	5.59±0.65	5.70±0.59	5.72±0.53	5.73±0.43
0.25	-6 dB width [mm] at 18 mm depth	1.01±0.91	0.44±0.62	0.25±0.24	0.21±0.04	0.21±0.03	0.20±0.03
	-6 dB width [mm] at 36 mm depth	2.28±1.31	0.93±0.75	0.53±0.40	0.42±0.26	0.39±0.21	0.29±0.02
	Contrast [dB]	3.34±1.26	5.18±0.73	5.60±0.63	5.66±0.63	5.65±0.60	5.73±0.43

TABLE II
RESOLUTION, CONTRAST, AND SOUND SPEED ERROR ACROSS THE SIX ABDOMINAL MAPS SHOWN IN FIGS. 3 AND 4

Case	Metrics	Map 1	Map 2	Map 3	Map 4	Map 5	Map 6
Ideal	-6 dB width [mm]–18 mm depth	0.21±0.02	0.57±0.84	0.20±0.02	0.20±0.02	1.29±1.59	0.20±0.02
	-6 dB width [mm]–36 mm depth	0.27±0.01	0.27±0.01	0.28±0.01	0.28±0.02	0.28±0.01	0.28±0.01
	Contrast [dB]	6.25	5.26	5.32	5.53	5.19	5.13
Before Correction	-6 dB width [mm]–18 mm depth	0.30±0.04	2.17±1.32	0.40±0.35	0.99±1.19	1.71±1.30	2.68±0.65
	-6 dB width [mm]–36 mm depth	0.36±0.13	1.36±1.18	0.92±0.80	2.19±0.92	1.94±1.44	1.16±0.75
	Contrast [dB]	6.24	4.29	4.52	2.37	4.11	3.85
$\gamma = 1.0$	-6 dB width [mm]–18 mm depth	0.24±0.01	0.72±0.84	0.25±0.04	0.24±0.03	0.96±1.03	0.81±0.82
	-6 dB width [mm]–36 mm depth	0.31±0.05	0.29±0.02	0.65±0.39	0.30±0.01	0.32±0.02	1.44±1.05
	Contrast [dB]	6.01	5.18	5.24	4.51	5.35	5.70
$\gamma = 0.5$	-6 dB width [mm]–18 mm depth	0.20±0.02	0.57±0.82	0.22±0.05	0.21±0.01	1.03±1.13	0.23±0.08
	-6 dB width [mm]–36 mm depth	0.28±0.01	0.28±0.01	0.30±0.03	0.30±0.01	0.29±0.02	0.44±0.19
	Contrast [dB]	6.20	5.37	5.00	4.93	4.77	5.38
$\gamma = 0.25$	-6 dB width [mm]–18 mm depth	0.20±0.02	0.56±0.82	0.20±0.02	0.20±0.01	0.89±0.96	0.20±0.02
	-6 dB width [mm]–36 mm depth	0.28±0.02	0.28±0.01	0.29±0.03	0.30±0.03	0.29±0.02	0.76±0.34
	Contrast [dB]	6.19	5.29	5.41	5.10	5.18	5.53

B. *Demonstration of the Iterative Correction Scheme*

Fig. 2 shows the IMPACT scheme used to estimate the sound speed and reconstruct the ultrasound image at each iteration in two different cases ((a) and (b)). The focusing of the ultrasound images improves with each iteration of IMPACT. This demonstration shows that while a large amount of aberration correction is achieved within the first iteration, successive iterations are needed to optimally measure the aberration and reconstruct the ultrasound image based on improved estimates of the sound speed profile. For $\gamma = 1.0,\ 0.5,\ 0.25$, Table I demonstrates the iterative improvement in point target resolution (-6 dB widths of point targets at 18 and 36 mm depth) and contrast over all 12 Gaussian-random aberrators as compared to the ideal correction using the exact ground-truth sound speed profiles. These results show that accurate sound speed estimates are not an absolute requirement for image quality improvement since resolution and contrast improve with each iteration of IMPACT.

C. *Impact of Priors on Sound Speed Reconstruction*

Fig. 3 demonstrates the ideal correction based on the ground-truth sound speed map and the actual correction using the IMPACT sound speed estimate ($\gamma = 1.0$, after 5 iterations) for each of the 6 abdominal maps. Despite the inaccuracy of the sound speed estimate when $\gamma = 1.0$, significant aberration corrections are achieved. Fig. 4 shows the IMPACT correction scheme using layered medium priors $\gamma = 0.5,\ 0.25$ for each of the 6 abdominal maps. Although the layered medium prior better reconstructs the axially varying component of sound speed, the improvement in aberration correction relative to the corrections with $\gamma = 1.0$ is much smaller. Table II shows the point target resolution, contrast, and CNR across the six abdominal maps before correction, after the ideal correction using the ground truth sound speed maps, and the IMPACT correction using $\gamma = 1.0,\ 0.5,\ 0.25$.

Another important factor in the IMPACT scheme is the choice of initial sound speed guess. In all examples shown so far, the initial sound speed guess used in all imaging cases is 1540 m/s; however, alternative choices for the initial sound speed impacts the depth placement of imaging targets, which can then affect the sound speed estimate. Fig. 5 shows the result of applying IMPACT ($\gamma = 0.25$) to abdominal maps 3 and 4 (case (a) and (b), respectively) when the initial sound speed guess is 1500, 1540, and 1580 m/s. The initial sound speed guess affects the depth placement of imaging targets both before and after aberration correction. These changes in the depth placement of the imaging target also have a corresponding effect on final sound speed estimate. As the initial sound speed guess increases, sound speed values in the final estimate also increase. However, there is a more subtle near-field effect that accompanies this increase in sound speed values. The lateral variation in the sound speed estimate near the transducer surface absorbs some of the curvature in the arrival time profile due to the bulk error in sound

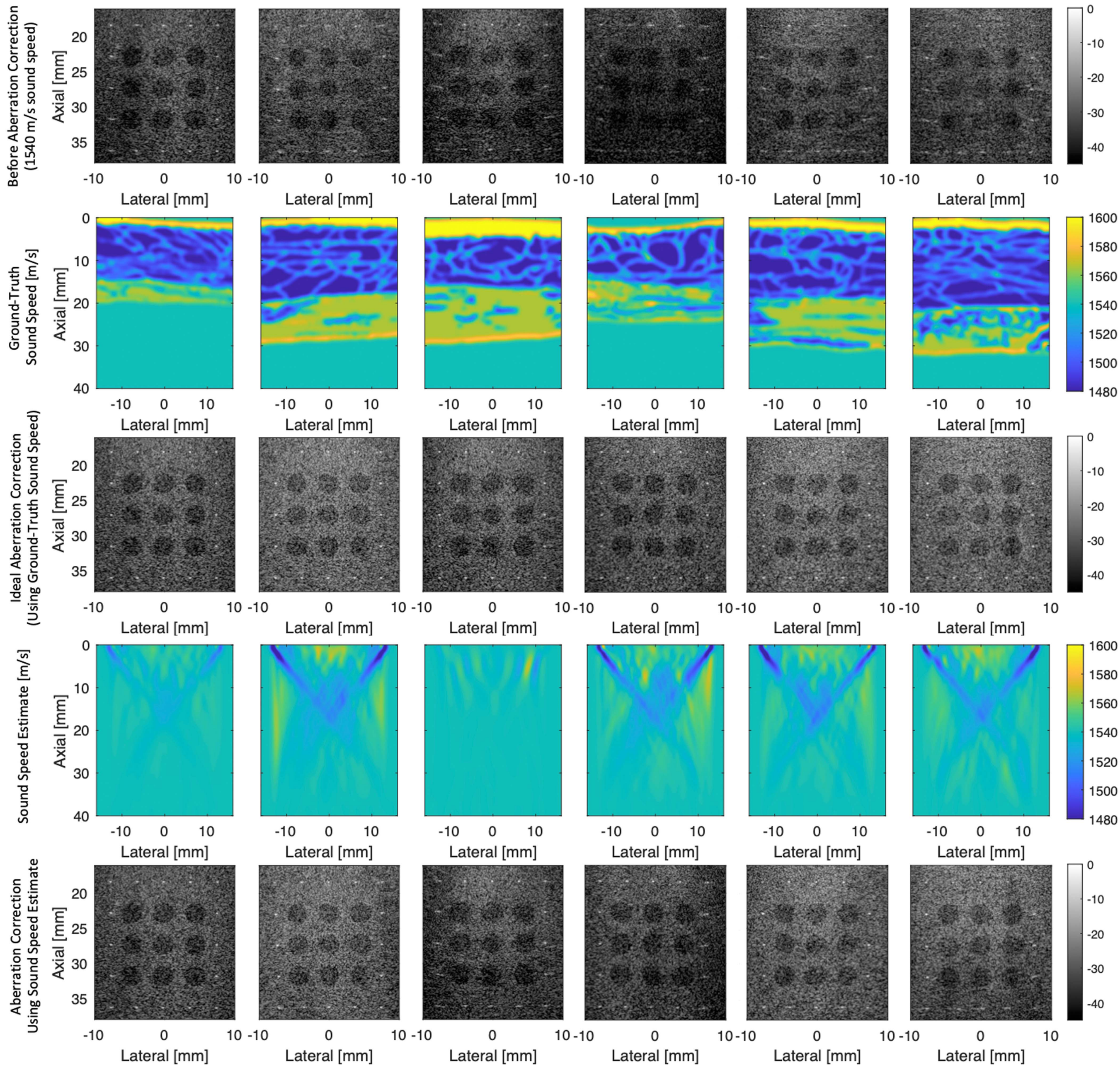

Fig. 3. Demonstration of IMPACT on Each Abdominal Map with a Non-Informative Prior ($\gamma = 1.0$) on Sound Speed. Each abdominal map was simulated in k-Wave. The aberration correction achieved using the ground truth sound speed and sound speed estimate after 5 iterations of IMPACT is shown. Despite the inaccuracy of the sound speed estimate, aberration corrections are achieved in each case. See Table II for the quantification of resolution, contrast, and sound speed estimation error.

speed. In both cases with an initial 1500 m/s sound speed model, the sound estimate near the transducer surface is highest at the edges of the array and lowest towards the center of the array. Conversely, when the initial sound speed model is 1580 m/s, the sound estimate near the transducer surface is lowest at the edges of the array but highest towards the center of the array.

We hypothesize that the laterally varying component of the sound speed estimate can often compensate for spherical aberrations resulting from a bulk sound speed error. Table III provides the point target resolution, contrast, CNR, and sound speed error for each of the results shown in Fig. 5. Although Table III shows an increase in the -6 dB width as the initial sound speed increases, this is the result of the increase in depth of each imaging target. To provide further supporting evidence for our hypothesis, the results of Fig. 5 are supplemented by the aberration delay maps shown in Fig. 6. These aberration delay maps are the result of applying the forward model to the ground-truth sound speed profile and the sound speed estimates obtained using each initial sound speed. The similarity in the resulting aberration delay profiles supports the conclusion that lateral variations in sound

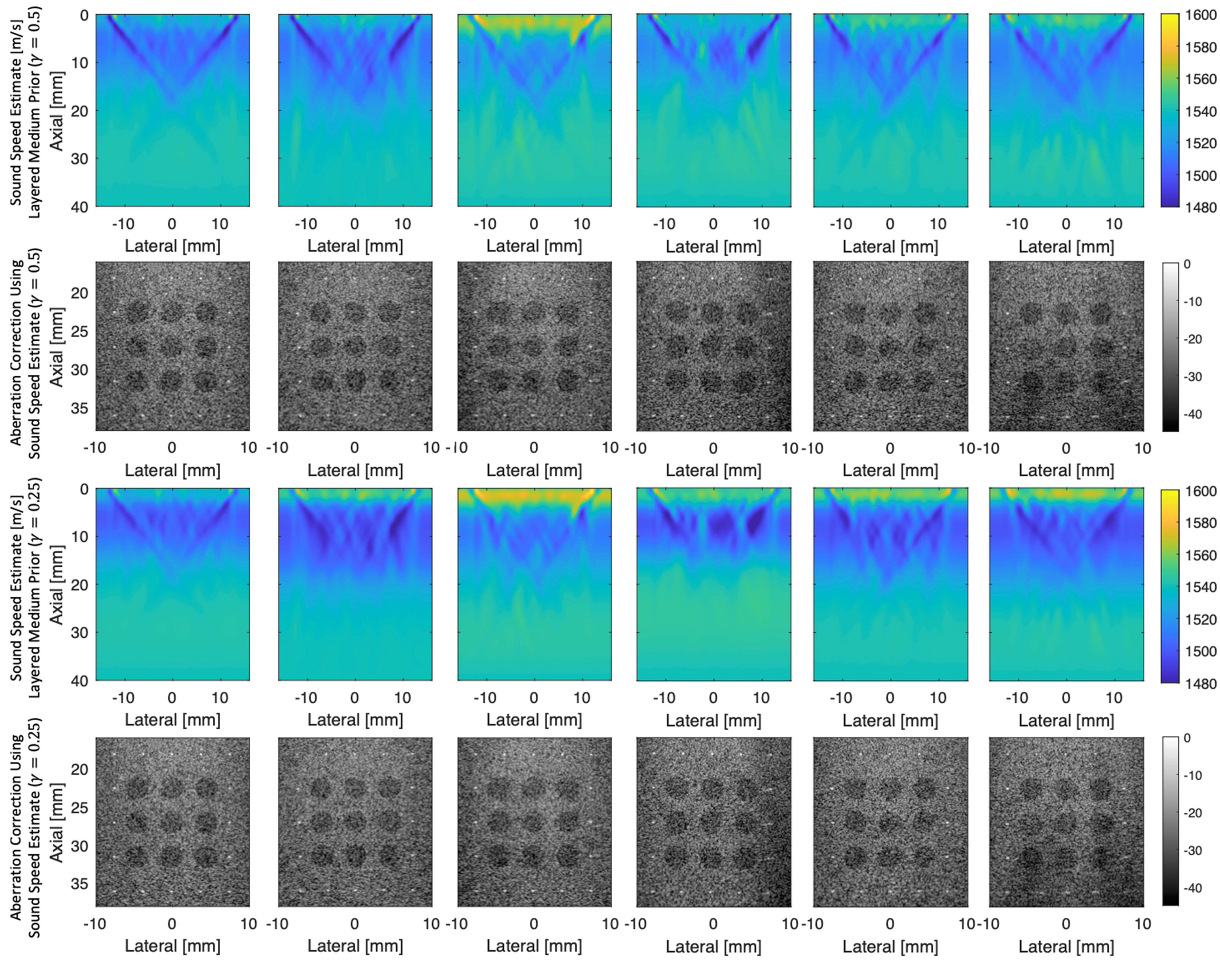

Fig. 4. Demonstration of IMPACT on Each Abdominal Map with Layered Priors ($\gamma = 0.5, 0.25$) on Sound Speed. The columns of this figure correspond to the k-Wave simulations of the abdominal maps in each column of Fig. 3. The layered medium priors improve measurement of axial variations in the sound speed profile. However, there is no significant improvement in the aberration corrections achieved in each case as a result of applying the layered priors. See Table II for the quantification of resolution, contrast, and sound speed estimation error.

TABLE III
RESOLUTION, CONTRAST, AND SOUND SPEED ERROR FOR ABDOMINAL MAPS 3 AND 4 [CASES (A) AND (B) IN FIG. 5]

Case	Metrics	Case (a)–Abdominal Map 3			Case (b)–Abdominal Map 4		
	Initial Sound Speed [m/s]	1500	1540	1580	1500	1540	1580
Before Correction	-6 dB width [mm] at 18 mm depth	0.34±0.13	0.40±0.35	0.39±0.19	0.81±0.44	0.99±1.19	1.03±0.85
	-6 dB width [mm] at 36 mm depth	1.20±1.04	0.92±0.80	0.93±1.14	2.43±1.42	2.19±0.92	2.15±0.94
	Contrast [dB]	3.40	4.52	5.05	1.80	2.37	2.35
After Correction	-6 dB width [mm] at 18 mm depth	0.20±0.03	0.20±0.03	0.21±0.03	0.20±0.02	0.20±0.01	0.21±0.02
	-6 dB width [mm] at 36 mm depth	0.28±0.02	0.29±0.03	0.31±0.03	0.29±0.03	0.31±0.03	0.32±0.03
	Contrast [dB]	5.56	5.41	5.50	5.32	5.10	5.10

speed play a much greater role on the final sound speed estimate than a spatially constant error in sound speed and ultimately results in similar corrections to the image.

D. Experimental Demonstration of IMPACT

Fig. 7 uses 3 alcohol-gelatin inclusions to perturb sound speed in a controlled manner to induce aberrations in the image. IMPACT reconstructs the sound speed profile over the alcohol inclusions and shows the corrected B-mode image. Wire target resolution and the visualization of the boundaries of the 3 hypoechoic lesions below the rows of wire targets improves as a result of aberration correction. Fig. 8 provides a more dramatic demonstration of aberration correction using 2 alcohol-gelatin inclusions (1 big and 1 small). The strong aberrations resulting from this asymmetric sound speed profile make estimation and correction far more difficult. Despite this increased difficulty, there are large improvements in wire target resolution and it becomes far easier to discern the 3 hypoechoic lesion below the point targets. Moving towards abdominal *in vivo* imaging

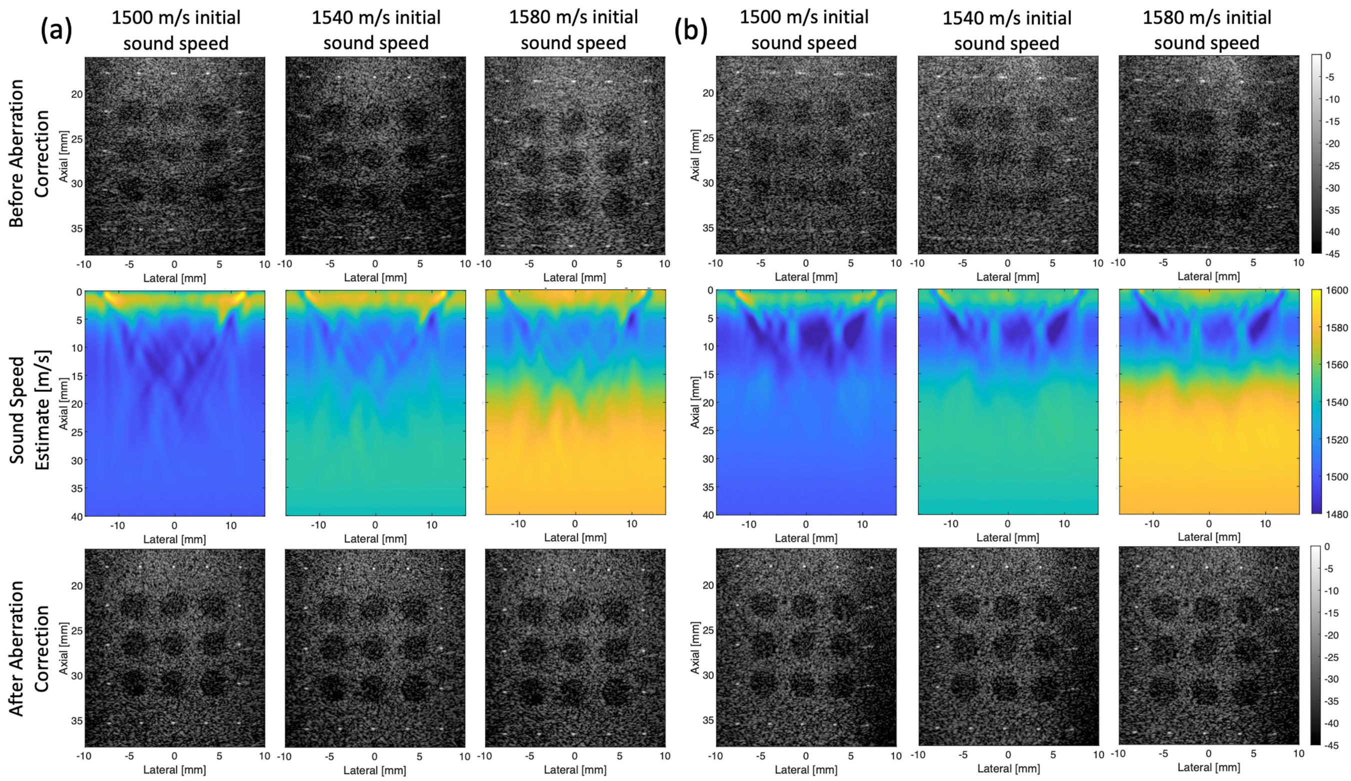

Fig. 5. Effect of Starting Sound Speed Model on IMPACT with a Layered Medium Prior ($\gamma = 0.25$) on Sound Speed. The choice of initial sound speed (1500, 1540, or 1580 m/s) has a significant impact on the sound speed reconstruction, but has little impact on the quality of the aberration correction. The only effect that the sound speed initialization has on the image is the depth placement of imaging targets. See Table III for the quantification of resolution, contrast, and sound speed estimation error. Cases (a) and (b) correspond to the 3 rd and 4th abdominal maps shown in Figs. 3 and 4.

applications, Fig. 9 shows the aberration correction resulting from 10 iterations of IMPACT when aberrating porcine abdominal tissue is placed on top of a phantom with 3 rows of point targets. The aberration correction is shown to improve point target resolution. Lastly, Fig. 10 demonstrates 3 examples of aberration correction in the rat abdomen. In each case, the overall image quality and resolution of structures on distal end of the liver appear to improve. The aberration correction in these examples is less dramatic because the sound speed variation in these tissues is less severe. Future work with channel data from a clinical scanner will be used to assess this technique in applications where aberration has a greater impact on image quality.

V. Discussion

This work demonstrates a method that can reconstruct sound speed variations in the medium from measured aberration delays to improve focusing in the image. Rather than relying on a single set of measured aberration delays to reconstruct sound speed, the image is iteratively refocused based on the running estimate of the sound speed to remeasure aberration delays and update the sound speed profile. This process implies a strong duality between aberration correction and sound speed estimation: the ability to estimate the sound speed profile in the medium is intrinsically tied to aberrations that can be corrected in the ultrasound image. The Bayesian prior $\boldsymbol{Q}(\gamma)$ can be used to enforce a layered medium structure that promotes a more accurate reconstruction of sound speed (see Fig. 4 and Table II) for layered structures, but the accuracy of the reconstruction degrades with depth regardless of the choice of γ and is highly dependent on the initial sound speed guess (see Fig. 5).

The duality between aberration correction and sound speed estimation provides several key insights into the ill-posed nature of sound speed estimation using pulse-echo measurements. The most fundamental challenge is related to the time-to-depth ambiguity [24], [25]. Creating an initial B-mode image requires a sound speed guess; however, the choice of sound speed affects the depth placement of imaging targets. Most tomographic reconstruction techniques [10], [11], [12], [22], [24] estimate the sound speed profile from shifts, or aberration delays, measured in the image. However, the aberration delay measurement may not be registered to the correct imaging point due the initial depth placement of the imaging target. A Fourier-domain analysis [22] of tomographic sound speed estimation shows that aberration delays do not retain sufficient information to estimate a spatially constant error in sound speed without first assuming that the error in sound speed is spatially constant. A spatially constant error in sound speed results in additional curvature of aberration delays, which is often well-approximated by a near-field phase screen [45]. Fig. 5 effectively demonstrates near-field effects similar to those demonstrated in [24]. Despite errors in

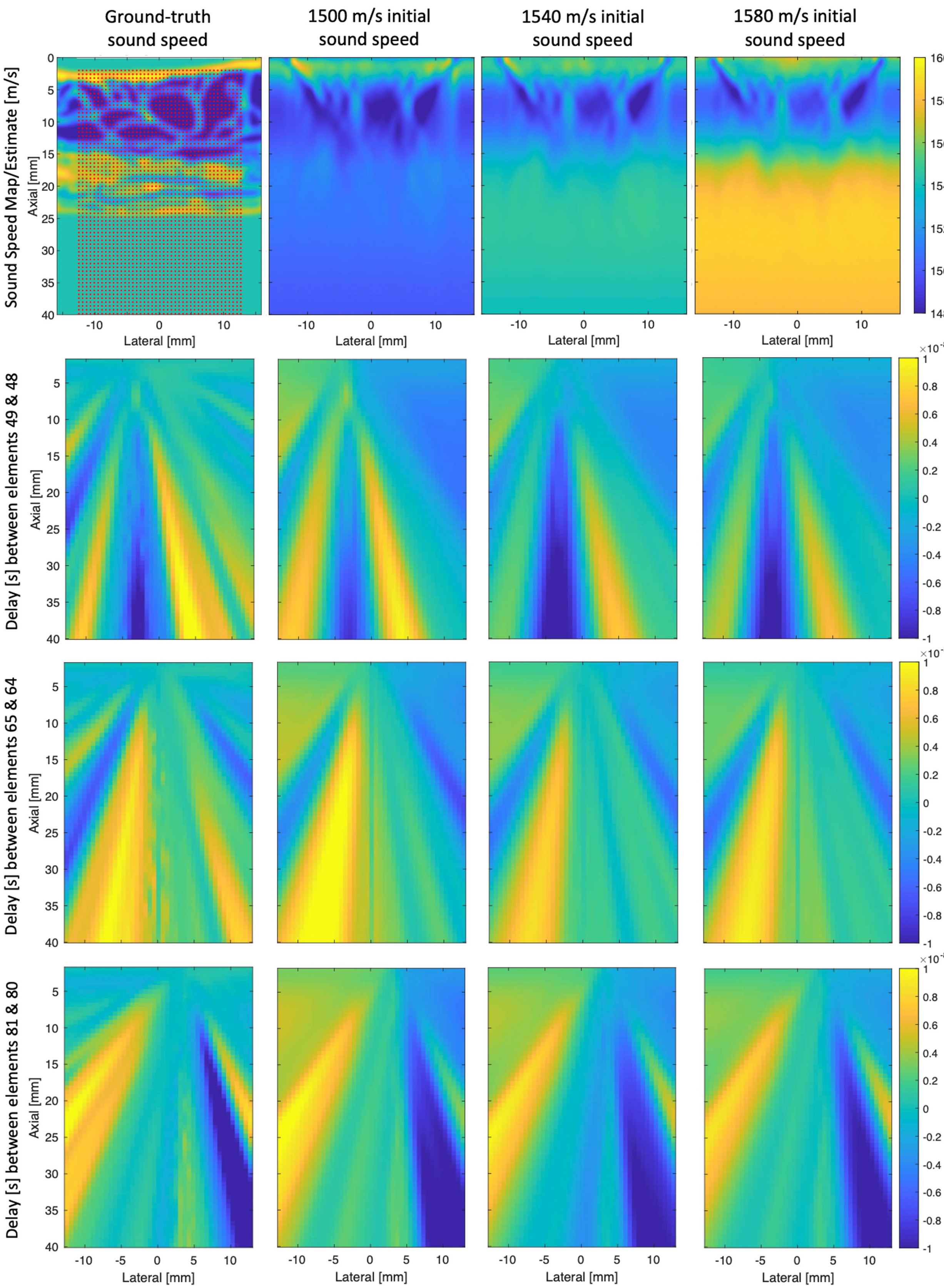

Fig. 6. Effect of Starting Sound Speed Model on Projected Aberration Delay Maps Using IMPACT with a Layered Medium Prior ($\gamma = 0.25$) on Sound Speed. This figure compares the delay maps obtained from the forward model using the ground truth sound speed distribution and the final estimated sound speed distribution obtained using each initial sound speed (1500, 1540, or 1580 m/s) in Fig. 5(b). Red dots on the ground-truth sound speed map indicate where the aberration delays were measured using the forward model.

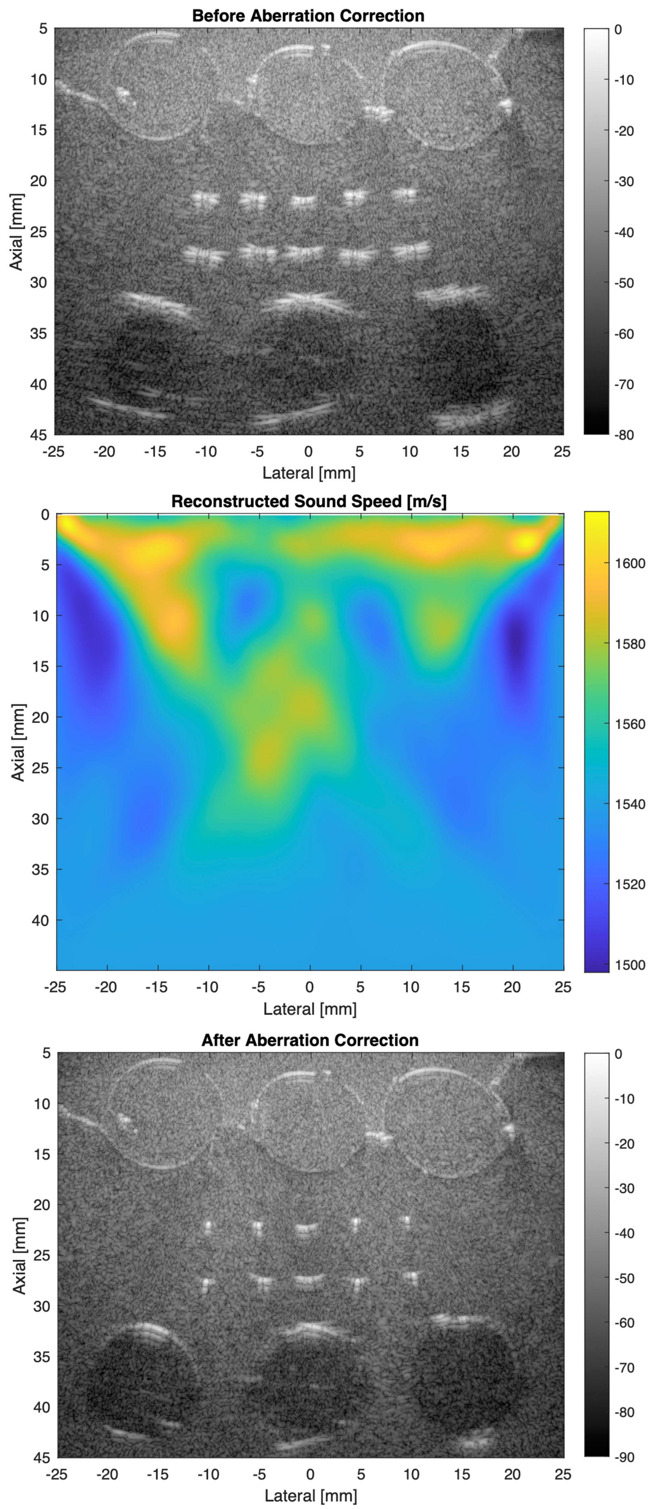

Fig. 7. Demonstration of IMPACT ($\gamma = 1.0$) in a Phantom with Three Alcohol Inclusions. Before aberration correction, the -6 dB beamwidths of the point targets were 1.89±0.86 mm; after aberration correction, the -6 dB beamwidths were 0.54±0.48 mm. Before aberration correction, the contrast of the three hypoechoic targets (from left to right) were 8.13, 2.99, and 8.73 dB; after correction, their contrast becomes 9.44, 7.61, and 11.50 dB. Note that the display dynamic range before aberration correction was 80 dB but was changed to 90 dB after aberration correction. This was done to maintain the overall brightness of the image due to the relative increase in the intensity of point targets in the image. Here, IMPACT is shown to improve both resolution and contrast in this phantom experiment.

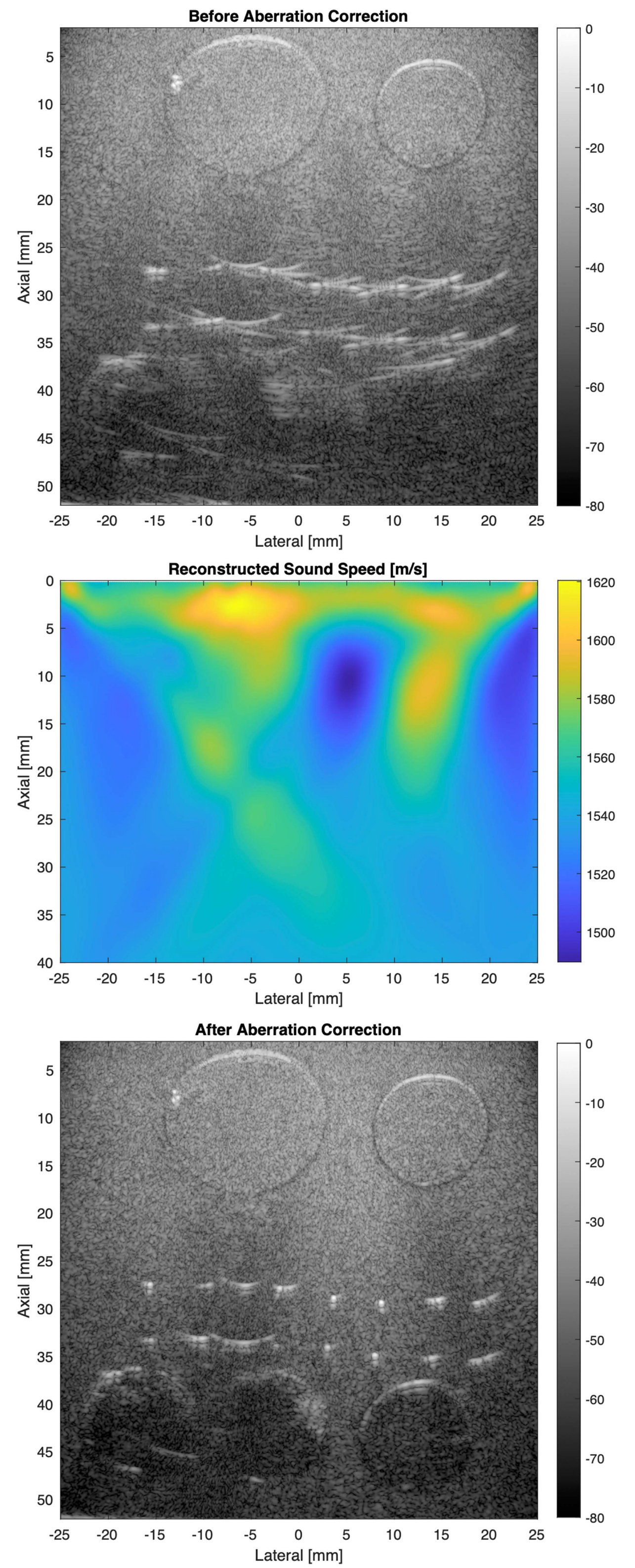

Fig. 8. Demonstration of IMPACT ($\gamma = 1.0$) in a Phantom with Two Alcohol Inclusions. Before aberration correction, the -6 dB beamwidths of the point targets were 2.81±1.88 mm; after aberration correction, the -6 dB beamwidths were 0.69±0.51 mm. Before aberration correction, the contrast of the three hypoechoic targets (from left to right) were 1.05, 0.05, and 7.25 dB; after correction, their contrast becomes 4.31, 10.07, and 8.53 dB. IMPACT is shown to improve both resolution and contrast in this phantom experiment.

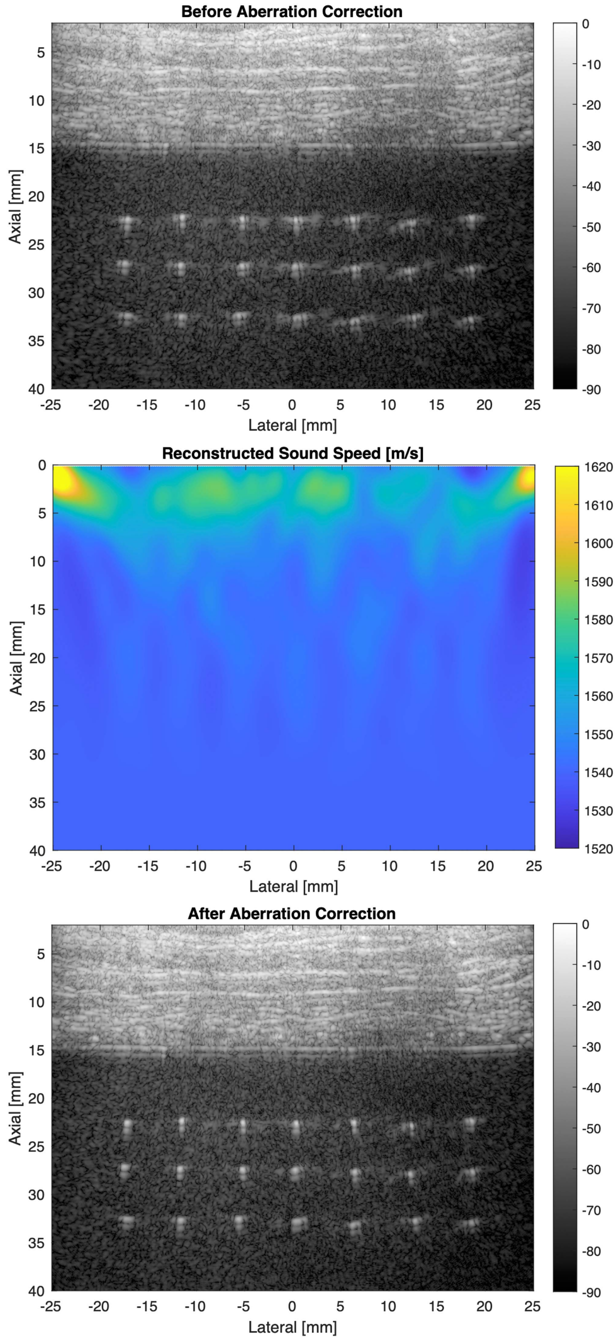

Fig. 9. Demonstration of IMPACT ($\gamma = 1.0$) in a Point Target Phantom with an Aberrating Porcine Sample. Before aberration correction, the -20 dB and -6 dB beamwidths of the point targets were 1.47±0.76 and 0.47±0.35 mm, respectively. After aberration correction, the -20 dB and -6 dB beamwidths were 0.89±0.36 and 0.42±0.29 mm, respectively. IMPACT is shown to improve imaging resolution in this phantom experiment as well.

the reconstructed sound speed, aberration correction results in equally well-focused images even though the depth placement of imaging targets can vary. This observation is similar to previous work where a simple midfield screen [30] corrects most of the aberration resulting from a spatially varying sound speed.

One potential way to reduce the dependence of the sound speed estimate on the initial sound speed model is to use a calibration phantom [11], [29]. We briefly describe the calibration procedure from [29]. Starting from an initial sound speed c_0, the slowness update $\Delta s(x,z)$ will update the slowness estimate to $s_{estim}(x,z) = \frac{1}{c_0} + \Delta s(x,z)$. However, as we have seen in Fig. 5, this slowness estimate will be biased by c_0. The authors of [29] instead estimate the slowness as $s_{estim}(x,z) = \left[\frac{1}{c_0} + \Delta s(x,z)\right] - \left[\frac{1}{\hat{c}_{cal}(x,z)} - \frac{1}{c_{cal}}\right]$, where c_{cal} is the true sound speed in a calibration phantom and $\hat{c}_{cal}(x,z)$ is an estimate of the sound speed in the calibration phantom when starting from an initial sound speed of c_0. The goal of this additional $\left[\frac{1}{\hat{c}_{cal}(x,z)} - \frac{1}{c_{cal}}\right]$ calibration term is to correct for biases caused by the initial sound speed c_0. If a similar calibration phantom approach had been used in Fig. 5, the sound speed reconstruction would appear to be less dependent on the initial sound speed model. However, this process may still be biased by the sound speed c_{cal} in the calibration phantom. For example, if $c_{cal} = c_0$, then $\left[\frac{1}{\hat{c}_{cal}(x,z)} - \frac{1}{c_{cal}}\right]$ should be very close to 0, and $s_{estim}(x,z)$ would remain biased by c_0. Therefore, it at least appears that the $\left[\frac{1}{\hat{c}_{cal}(x,z)} - \frac{1}{c_{cal}}\right]$ calibration term requires that c_{cal} be close to the average sound speed of the sample being imaged so that the calibration results in the desired correction. Unfortunately, the parameters of this calibration approach were not fully investigated in the prior work [29].

In contrast, previous work on coherence-based sound speed estimators [9], [14], [18], [20] can accurately estimate the sound speed profile in a layered medium without any biases resulting from the time-to-depth ambiguity or using a calibration phantom to provide an absolute sound speed reference. In a perfectly layered medium, focusing at each imaging point is well-approximated by an effective average sound speed up to that point. The optimal focusing sound speed may be found by maximizing coherence at each imaging point. This effectively provides a simultaneous registration of sound speed and imaging depth. However, coherence-based approaches quickly become inaccurate in the presence of a laterally varying sound speed profile and can often result in poor image corrections [9]. To overcome the limitations of the prior work [9], this work has demonstrated an iterative scheme that corrects for aberrations in a laterally-varying sound speed medium. In contrast to other tomographic sound speed estimators that rely on a single observation of aberration delays to reconstruct the sound speed profile, we observe a new set of aberration delays with each update to the sound speed model to refine the estimate and achieve optimal focusing in the image. Fig. 2 demonstrates the importance of this approach. Although the biggest improvements are seen in the first iteration, additional iterations are necessary to improve focusing in the image. This is mostly because our linearized forward model (slowness profile to aberration delays) cannot account for: 1) inaccuracies in the depth placement of the imaging target, 2) decorrelation between transmitters caused by aberrations over the receive aperture (especially on the first few iterations of IMPACT) resulting from an implicit integration over mid-angles [11] in our approach, 3) refraction (e.g., the error between predicted and measured aberration delay in Fig. 1), and 4) diffraction. IMPACT reduces the decorrelation between

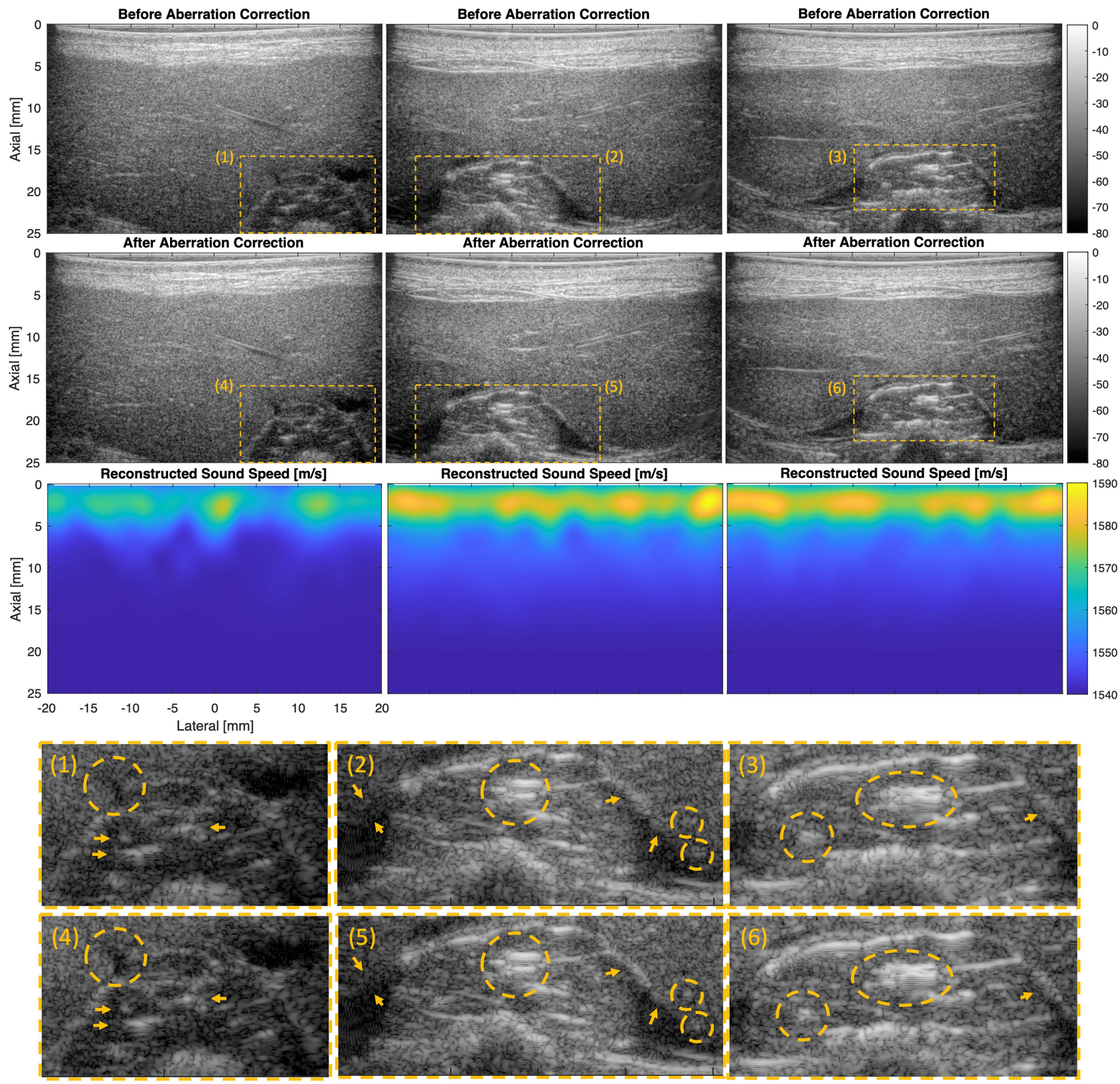

Fig. 10. Demonstration of IMPACT ($\gamma = 0.5$) in the Abdomen of Obese Zucker Rats. A layered-medium prior ($\gamma = 0.5$) was used to take advantage of the layered structure of the abdomen. In each case, aberration correction improves the focusing of structures at the distal end of the liver. Regions-of-interest (1)-(6) are expanded and annotated to highlight parts of the image where the aberration correction improves image quality.

transmitters as the sound speed estimate becomes more accurate and partially corrects for refractive effects as evidenced by the agreement in projected aberration delays in Fig. 6. In all k-Wave simulations shown (Figs. 2, 3, and 4), resolution and contrast converge to their ideal values in about 3-5 iterations of IMPACT. However, in the phantom experiments with the alcohol inclusions (Figs. 7 and 8), significant improvements could still be seen past the 5th iteration. The number of iterations required ultimately depends on the nonlinear relationship between sound speed in the medium and aberration measured. The larger the variation in sound speed, the more nonlinear this relationship becomes, and the more iterations are required for convergence to be achieved. On an Intel Core$^{\text{TM}}$ i5-10400 CPU @2.90 GHz processor, all five iterations of IMPACT (as currently implemented in MATLAB 2021b) require an approximate total of 4000 seconds for each of the k-Wave simulations used in this study. Note that this implementation of IMPACT has not been optimized for speed. The major computational burden comes from the Fourier split-step method itself. However, a parallelized GPU implementation could significantly accelerate this approach.

The ultimate vision behind this work is to provide a robust solution to sound speed estimation and aberration correction for clinical *in vivo* ultrasound imaging. The main challenges in extending this work to a clinical setting is the presence of reverberation clutter and strong fluctuations in backscatter intensity. Coherent reverberation can bias the aberration delay measurement based on signals from a shallow reflector that are misregistered deeper in the image. Previous coherence-based approaches were more robust to reverberation clutter because coherence imaging does not require the measurement of aberration delays between individual element pairs. Direction-of-arrival filtering [43] can mitigate reverberation for the purposes of aberration delay measurements, but it does not fully remove the impact of reverberation clutter. Aperture domain model image reconstruction (ADMIRE) [46] has been shown to fully suppress reverberation clutter in channel data; however, it remains unclear how well ADMIRE performs in the presence of aberrations induced by a spatially varying sound speed profile. ADMIRE may need to be revised to accounts for sound speed heterogeneity in the medium.

Another source of error is the heterogeneity of backscatter. A strong off-axis reflector may result in the measurement of aberration delays from neighboring locations in the image. Although median filtering reduces outliers resulting from off-axis scattering, ray tomography is fundamentally unable to account for diffraction during sound speed reconstruction. By using Fourier split-step migration to reconstruct the image based on the sound speed estimate, this work presents a diffraction-based imaging model that uses a ray-based time-of-flight model to reconstruct sound speed. A refraction-corrected or bent-ray reconstruction could theoretically improve the sound speed estimate, but a practical implementation is limited by numerical instabilities from fluctuations in the sound speed estimate near the transducer surface.

Additional improvements to the methodology presented in this work could include using time shift estimates from multiple element offsets and using time-domain cross correlation instead of phase shift measurements to calculate time shifts. Our work only uses time shifts measured between neighboring elements for sound speed tomography. However, time shifts could have been measured between elements that were further apart. This approach is equivalent to the multi-lag least squares (MLLS) cross correlation approach [47], [48], where element pairs of multiple different offsets (or lags) were used in an overdetermined least squares problem to estimate aberration delays. However, special care needs to be taken in order to assure that these additional measurements do not add jitter to the final estimate because the received signal decorrelates with larger element offsets. Instead, our approach uses a transmit apodization [44] that optimizes the correlation of signals on neighboring elements to improve aberration delay estimation. Additionally, our approach uses phase shift estimation rather than time-domain cross correlation to estimate aberration delays. This assumes that the phase shift is less than π between neighboring receive elements. This is a fair assumption for medical ultrasound imaging because most probes are designed to avoid grating lobes, which are the result of having phase shifts larger than π between transducer elements. Time-domain cross correlation, or block matching, may be more accurate than phase shift estimation but is far more expensive. Furthermore, time-domain cross correlation may still be susceptible to cycle-skipping in the same way that the phase shift estimation is problematic for shifts larger than π if the waveforms are not shifted by a sufficiently large amount.

Recent work [33] proposes to use a fully diffractive approach by using Fourier split-step migration to both focus the image and reconstruct the sound speed profile. Rather than estimate aberration delays from the image, this new approach would directly back-project the discrepancy between images $I_i(x,z;t)$ and $I_{i+1}(x,z;t)$ to reconstruct slowness using Fourier split-step migration. In seismic imaging, this approach is also known as wave-equation migration velocity analysis (WEMVA) [49], [50]. WEMVA has several advantages over ray tomography. First, by directly modeling discrepancies in the image, WEMVA can fully account for the heterogeneities in backscatter that a simple time-of-flight model cannot account for. Second, unlike ray tomography, WEMVA is a form of diffraction tomography that enables greater sensitivity to perturbations in the image, which benefits both sound speed estimation and phase aberration correction. By incorporating diffraction into the image formation model, this work is a steppingstone towards the implementation of WEMVA into pulse-echo ultrasound imaging. Future work will replace ray tomography with diffraction tomography using WEMVA.

VI. Conclusion

Sound speed estimates in a spatially varying medium can be used to improve the focusing of signals, thereby significantly increasing the resolution of ultrasound images. The main limitation of our prior work was the inability to robustly estimate sound speed in a laterally varying medium. This work overcomes this limitation by employing at iterative scheme whereby aberrations in the image are used to update the sound speed estimate and re-image the sample. Simulations, phantoms, and *in vivo* experiments show significant improvements in image quality when this iterative approach is used to correct for aberrations in the image. In order to make our efforts more accessible to the broader research community, we provide sample code and multistatic synthetic aperture channel data from 1) a k-Wave simulation, 2) an in-vitro phantom, 3) the abdomen of an obese Zucker rat at https://github.com/rehmanali1994/IMPACT (DOI: 10.5281/zenodo.7178906).

VI. Acknowledgment

The authors would like to thank Drs. Joseph Jennings and Biondo Biondi from the Department of Geophysics, Dr. Peter Kitanidis from Civil and Environmental Engineering, and Dr. Anthony Podkowa from the Department of Radiology at Stanford University for their valuable scientific discourse. The authors would also like to thank Dr. Kevin Parker from the Department of Electrical and Computer Engineering, Dr. Stephen McAleavey from the Department of Biomedical Engineering, and Dr. Deborah Rubens from the Department of Imaging Sciences at the University of Rochester for their insights.

REFERENCES

[1] R. S. Cobbold, *Foundations of Biomedical Ultrasound*. Oxford, U.K.: Oxford Univ. Press, 2006.

[2] S. Flax and M. Donnell, "Phase-aberration correction using signals from point reflectors and diffuse scatterers: Basic principles," *IEEE Trans. Ultrason., Ferroelectr., Freq. Control*, vol. 35, no. 6, pp. 758–767, Nov. 1988.

[3] D. Rachlin, "Direct estimation of aberrating delays in pulse-echo imaging systems," *J. Acoustical Soc. Amer.*, vol. 88, no. 1, pp. 191–198, 1990.

[4] G. Trahey, D. Zhao, J. A. Miglin, and S. W. Smith, "Experimental results with a real-time adaptive ultrasonic imaging system for viewing through distorting media," *IEEE Trans. Ultrason., Ferroelectr., Freq. Control*, vol. 37, no. 5, pp. 418–427, Sep. 1990.

[5] H.-M. Schwab, A. Ihrig, D. Depke, S. Hermann, M. Schäfers, and G. Schmitz, "Aberration correction in photoacoustic imaging using paraxial backpropagation," in *Proc. IEEE Int. Ultrasonics Symp.*, 2017, pp. 1–4.

[6] H.-M. Schwab and G. Schmitz, "Full-wave ultrasound reconstruction with linear arrays based on a Fourier split-step approach," in *Proc. IEEE Int. Ultrasonics Symp.*, 2018, pp. 1–4.

[7] C. Jiang, Y. Li, K. Xu, and D. Ta, "Full-matrix phase shift migration method for transcranial ultrasonic imaging," *IEEE Trans. Ultrason., Ferroelectr., Freq. Control*, vol. 68, no. 1, pp. 72–83, Jan. 2021.

[8] R. Ali and J. J. Dahl, "Distributed phase aberration correction techniques based on local sound speed estimates," in *Proc. IEEE Int. Ultrasonics Symp.*, 2018, pp. 1–4.

[9] R. Ali, T. Brevett, D. Hyun, L. L. Brickson, and J. J. Dahl, "Distributed aberration correction techniques based on tomographic sound speed estimates," *IEEE Trans. Ultrason., Ferroelectr., Freq. Control*, vol. 69, no. 5, pp. 1714–1726, May 2022.

[10] R. Rau, D. Schweizer, V. Vishnevskiy, and O. Goksel, "Speed-of-sound imaging using diverging waves," *Int. J. Comput. Assist. Radiol. Surg.*, vol. 16, no. 7, pp. 1201–1211, 2021.

[11] P. Stähli, M. Kuriakose, M. Frenz, and M. Jaeger, "Improved forward model for quantitative pulse-echo speed-of-sound imaging," *Ultrasonics*, vol. 108, 2020, Art. no. 106168.

[12] M. Jaeger, G. Held, S. Peeters, S. Preisser, M. Grünig, and M. Frenz, "Computed ultrasound tomography in echo mode for imaging speed of sound using pulse-echo sonography: Proof of principle," *Ultrasound Med. Biol.*, vol. 41, no. 1, pp. 235–250, 2015.

[13] C. Yoon, Y. Lee, J. H. Chang, T.-K. Song, and Y. Yoo, "In vitro estimation of mean sound speed based on minimum average phase variance in medical ultrasound imaging," *Ultrasonics*, vol. 51, no. 7, pp. 795–802, 2011.

[14] M. E. Anderson and G. E. Trahey, "The direct estimation of sound speed using pulse–echo ultrasound," *J. Acoustical Soc. Amer.*, vol. 104, no. 5, pp. 3099–3106, 1998.

[15] H.-C. Shin, R. Prager, H. Gomersall, N. Kingsbury, G. Treece, and A. Gee, "Estimation of average speed of sound using deconvolution of medical ultrasound data," *Ultrasound Med. Biol.*, vol. 36, no. 4, pp. 623–636, 2010.

[16] X. Qu, T. Azuma, J. T. Liang, and Y. Nakajima, "Average sound speed estimation using speckle analysis of medical ultrasound data," *Int. J. Comput. Assist. Radiol. Surg.*, vol. 7, no. 6, pp. 891–899, 2012.

[17] M. E. Anderson, M. S. McKeag, R. C. Gauss, M. S. C. Soo, and G. Trahey, "Application of sound speed estimation and mapping to multi-layer media and in vivo data," in *Proc. IEEE Ultrasonics Symp.*, 1998, pp. 1393–1396.

[18] M. Imbault et al., "Ultrasonic fat fraction quantification using in vivo adaptive sound speed estimation," *Phys. Med. Biol.*, vol. 63, no. 21, 2018, Art. no. 215013.

[19] M. Jakovljevic et al., "Local speed of sound estimation in tissue using pulse-echo ultrasound: Model-based approach," *J. Acoust. Soc. Amer.*, vol. 144, no. 1, pp. 254–266, 2018.

[20] R. Ali et al., "Local sound speed estimation for pulse-echo ultrasound in layered media," *IEEE Trans. Ultrason., Ferroelectr., Freq. Control*, vol. 69, no. 2, pp. 500–511, Feb. 2022.

[21] C. H. Dix, "Seismic velocities from surface measurements," *Geophysics*, vol. 20, no. 1, pp. 68–86, 1955.

[22] A. S. Podkowa and M. L. Oelze, "The convolutional interpretation of registration-based plane wave steered pulse-echo local sound speed estimators," *Phys. Med. Biol.*, vol. 65, no. 2, 2020, Art. no. 025003.

[23] A. Podkowa and M. Oelze, "Echo-mode aberration tomography: Sound speed imaging with a single linear array," *J. Acoust. Soc. Amer.*, vol. 145, no. 3, pp. 1859–1859, 2019.

[24] A. S. Podkowa, "Spatiotemporal excitation sequence manipulation and processing for Doppler ultrasound and pulse-echo sound speed imaging applications," Ph.D. dissertation, Univ. Illinois Urbana-Champaign, Champaign, IL, USA, 2020.

[25] S. H. Bickel, "Velocity-depth ambiguity of reflection traveltimes," *Geophysics*, vol. 55, no. 3, pp. 266–276, 1990.

[26] L. Lines, "Ambiguity in analysis of velocity and depth," *Geophysics*, vol. 58, no. 4, pp. 596–597, 1993.

[27] H. J. Tieman, "Investigating the velocity-depth ambiguity of reflection traveltimes," *Geophysics*, vol. 59, no. 11, pp. 1763–1773, 1994.

[28] W. S. Ross, "The velocity-depth ambiguity in seismic traveltime data," *Geophysics*, vol. 59, no. 5, pp. 830–843, 1994.

[29] M. Jaeger et al., "Pulse-echo speed-of-sound imaging using convex probes," *Phys. Med. Biol.*, vol. 67, no. 21, 2022, Art. no. 215016.

[30] J. C. Tillett, J. P. Astheimer, and R. C. Waag, "A model of distributed phase aberration for deblurring phase estimated from scattering," *IEEE Trans. Ultrason., Ferroelectr., Freq. Control*, vol. 57, no. 1, pp. 214–228, Jan. 2010.

[31] M. Jaeger, E. Robinson, H. G. Akarçay, and M. Frenz, "Full correction for spatially distributed speed-of-sound in echo ultrasound based on measuring aberration delays via transmit beam steering," *Phys. Med. Biol.*, vol. 60, no. 11, pp. 4497–4515, 2015.

[32] R. Rau, D. Schweizer, V. Vishnevskiy, and O. Goksel, "Ultrasound aberration correction based on local speed-of-sound map estimation," in *Proc. IEEE Int. Ultrasonics Symp.*, 2019, pp. 2003–2006.

[33] R. Ali, "Open-source full-waveform ultrasound computed tomography based on the angular spectrum method using linear arrays," *Proc SPIE*, vol. 12038, pp. 187–205, 2022.

[34] U. Vyas and D. Christensen, "Ultrasound beam simulations in inhomogeneous tissue geometries using the hybrid angular spectrum method," *IEEE Trans. Ultrason., Ferroelectr., Freq. Control*, vol. 59, no. 6, pp. 1093–1100, Jun. 2012.

[35] C. Kasai, K. Namekawa, A. Koyano, and R. Omoto, "Real-time two-dimensional blood flow imaging using an autocorrelation technique," *IEEE Trans. Sonics Ultrasonics*, vol. 32, no. 3, pp. 458–464, May 1985.

[36] P. Sava and S. Fomel, "Time-shift imaging condition in seismic migration," *Geophysics*, vol. 71, no. 6, pp. S209–S217, 2006.

[37] T. D. Mast, L. M. Hinkelman, M. J. Orr, V. W. Sparrow, and R. C. Waag, "Simulation of ultrasonic pulse propagation through the abdominal wall," *J. Acoustical Soc. Amer.*, vol. 102, no. 2, pp. 1177–1190, 1997.

[38] B. E. Treeby and B. T. Cox, "k-wave: Matlab toolbox for the simulation and reconstruction of photoacoustic wave fields," *J. Biomed. Opt.*, vol. 15, no. 2, 2010, Art. no. 021314.

[39] R. Y. Chiao, L. J. Thomas, and S. D. Silverstein, "Sparse array imaging with spatially-encoded transmits," in *Proc. IEEE Ultrasonics Symp. Proc An Int. Symp.*, 1997, pp. 1679–1682.

[40] A. V. Telichko et al., "Noninvasive estimation of local speed of sound by pulse-echo ultrasound in a rat model of nonalcoholic fatty liver," *Phys. Med. Biol.*, vol. 67, no. 1, 2022, Art. no. 015007.

[41] J. R. Cook, R. R. Bouchard, and S. Y. Emelianov, "Tissue-mimicking phantoms for photoacoustic and ultrasonic imaging," *Biomed. Opt. Exp.*, vol. 2, no. 11, pp. 3193–3206, 2011.

[42] E. L. Madsen, J. A. Zagzebski, R. A. Banjavie, and R. E. Jutila, "Tissue mimicking materials for ultrasound phantoms," *Med. Phys.*, vol. 5, no. 5, pp. 391–394, 1978.

[43] J. J. Dahl and T. J. Feehan, "Direction of arrival filters for improved aberration estimation," *Ultrason. Imag.*, vol. 30, no. 1, pp. 1–20, 2008.

[44] R. Ali et al., "Distributed aberration correction in handheld ultrasound based on tomographic estimates of the speed of sound," in *Proc SPIE*, 2023.

[45] H. Bendjador et al., "The SVD beamformer with diverging waves: A proof-of-concept for fast aberration correction," *Phys. Med. Biol.*, vol. 66, no. 18, 2021, Art. no. 18LT01.

[46] K. Dei and B. Byram, "The impact of model-based clutter suppression on cluttered, aberrated wavefronts," *IEEE Trans. Ultrason., Ferroelectr., Freq. Control*, vol. 64, no. 10, pp. 1450–1464, Oct. 2017.

[47] D.-L. Liu and R. C. Waag, "Correction of ultrasonicwavefront distortion using backpropagation and a reference waveform method for time-shift compensation," *J. Acoust. Soc. Amer.*, vol. 96, no. 2, pp. 649–660, 1994.

[48] E. González, N. Sheth, B. Castañeda, J. Dahl, and R. Lavarello, "Accuracy of backscatter coefficient estimation in aberrating media using different phase aberration correction strategies-a simulation study," in *Proc. IEEE Int. Ultrasonics Symp.*, 2014, pp. 2438–2441.

[49] P. Sava and B. Biondi, "Wave-equation migration velocity analysis. I. Theory," *Geophysical Prospecting*, vol. 52, no. 6, pp. 593–606, 2004.

[50] F. Perrone, P. Sava, C. Andreoletti, and N. Bienati, "Linearized wave-equation migration velocity analysis by image warping," *Geophysics*, vol. 79, no. 2, pp. S35–S46, 2014.

Rehman Ali received the B.S. degree in biomedical engineering from the Georgia Institute of Technology, Atlanta, GA, USA, in 2016, the M.S. degree in computational & mathematical engineering and the Ph.D. degree in electrical engineering from Stanford University, Palo Alto, CA, USA, in 2020 and 2022, respectively. He is currently with the University of Rochester, Rochester, NY, USA, with the the Laboratory of Dr. Nebojsa Duric to develop waveform inversion reconstruction techniques for imaging acoustic tissue properties using ultrasound computed tomography. His research interests include signal processing, inverse problems, computational modeling of acoustics, and real-time beamforming algorithms.

Trevor M. Mitcham received the B.S. degree in bioengineering from Rice University, Houston, TX, USA, in 2012, and the Ph.D. degree in medical physics from The University of Texas MD Anderson Cancer Center UTHealth Graduate School of Biomedical Sciences, Houston, TX, in 2021. He is currently with the University of Rochester, Laboratory of Dr. Nebojsa Duric developing a research ultrasound system for use with ultrasound computed tomography. His research interests include ultrasound-mediated molecular imaging, photoacoustic imaging, and ultrasound phantom development.

Melanie Singh received the B.E. degree in biomedical engineering from Hofstra University, Hempstead, NY, USA, in 2021. Her main research focuses on ultrasound tomography. She is currently working twoard the Ph.D. degree with the University of Rochester, Rochester, NY, USA, under Dr. Nebojsa Duric developing a medical ultrasound tomography system for brain imaging.

Marvin M. Doyley (Senior Member, IEEE) received the Ph.D. degree in biophysics from the University of London, London, U.K., in 2000. From 2000 to 2001, he was with the Thorax Center, Experimental Echocardiography Department, Erasmus University, Rotterdam, The Netherlands. From 2001 to 2008, he was a Research Faculty Member with the Thayer School of Engineering, Dartmouth College, Hanover, NH, USA. In 2008, he joined the Department of Electrical and Computer Engineering with the University of Rochester, Rochester, NY, USA, where is he currently the Department Chair and Professor (with joint appointments in biomedical engineering and imaging sciences. His research interests include vascular elastography, elastographic imaging, harmonic imaging, and surrogate biomarkers for guiding pancreatic cancer treatment.

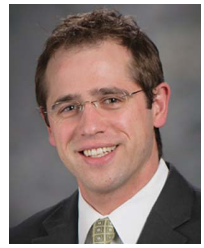

Richard R. Bouchard received the B.S. degree in biomedical and electrical engineering and cultural anthropology from Duke University, Durham, NC, USA, in 2004, and the Ph.D. degree in biomedical engineering from Duke University in 2010. He completed a Postdoctoral Fellowship with the Ultrasound Imaging and Therapeutics Research Laboratory, University of Texas at Austin, Austin, TX, USA, in 2012. He is currently an Associate Professor with the Department of Imaging Physics with the University of Texas MD Anderson Cancer Center where he directs the Photoacoustic Imaging Research Lab and is a Core Leader for ultrasound imaging in MD Anderson's Small Animal Imaging Core Facility. His research interests include preclinical and clinical photoacoustic-ultrasonic imaging and ultrasound-based elasticity imaging.

Jeremy J. Dahl (Senior Member, IEEE) received the B.S. degree in electrical engineering from the University of Cincinnati, Cincinnati, OH, USA, in 1999, and the Ph.D. degree in biomedical engineering from Duke University, Durham, NC, USA, in 2004. He is currently an Associate Professor with the Department of Radiology, Stanford University, Stanford, CA, USA. His research interests include beamforming, coherence and noise in ultrasonic imaging, speed of sound estimation, and ultrasound radiation force imaging technology.

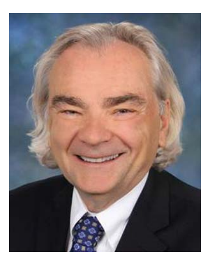

Nebojsa Duric received the Ph.D. degree in astrophysics from the University of Toronto, Toronto, ON, Canada. Following his postdoctoral work with the University of British Columbia, Vancouver, BC, Canada, he joined the Faculty with the University of New Mexico, Albuquerque, NM, USA. After a 20-year astrophysics career in radio astronomy, he began his new career in medical imaging, first with Karmanos Cancer Institute in Michigan and currently with the University of Rochester, Rochester, NY, USA, where he is a Professor and the Vice Chair for Research with Imaging Sciences Department. His research interests include ultrasound tomography (UST) with clinical applications to breast imaging. In 2010, he co-founded Delphinus Medical Technologies where he guided the R&D efforts in his role as a Chief Technology Officer. He was the recipient of the Michigan Innovator of the Year Award from the state of Michigan and a Distinguished Innovator Award from Wayne State University, recognizing innovation and achievement for his role in development of ultrasound tomography. He was also named a Hero of Breast Cancer by the Detroit Chapter of Race for the Cure, recognizing excellence in breast cancer research and education.